JOURNAL OF GEOPHYSICAL RESEARCH, VOL. 96, NO. C6, PAGES 10,453–10,466, JUNE 15, 1991

Ocean Wave Spectral Distortion in Airborne Synthetic Aperture Radar Imagery During the Norwegian Continental Shelf Experiment of 1988

CLIFFORD L. RUFENACH, ROBERT A. SHUCHMAN, AND NORMAN P. MALINAS

Center for Earth Sciences, Environmental Research Institute of Michigan, Ann Arbor

JOHNNY A. JOHANNESSEN

Nansen Remote Sensing Center, Bergen, Norway

C band radar images of ocean gravity waves off the Norwegian coast were processed into one-dimensional azimuth spectra. These spectra were used to measure the azimuth spectral (width) cutoff on the basis of a least squares fit to a Gaussian spectral shape. The widths were calculated for a range of wave heights (2–5 m) and wind speeds (2–18 m/s) during 3 days in March, 1988. Velocity smearing (σ_v) estimates were extracted, independent of R/V and incidence angle, based on an imaging model and the measured azimuth cutoffs with σ_v values varying from 0.4 to 0.7 m/s. Quantitative velocity smearing estimates are important as input to models describing the distortion in wave imagery. We propose a first-order model which neglects velocity bunching for ocean swell with peak wavelengths longer than about 250 m. This model is offered as a first estimate of when ocean wave swell will be detected by the C band SAR on board the ERS 1 spacecraft. The model predicts that this swell will be imaged under light winds of the order of 2–4 m/s. Higher wind speeds cause larger smearing, which may result in significant distortion of the imaged swell provided that the swell is traveling near the direction of the spacecraft ground track.

1. INTRODUCTION

Airborne synthetic aperture radar (SAR) measurements were acquired off the coast of Norway in March 1988 during the Norwegian Continental Shelf Experiment (NORCSEX '88). These C band SAR images detected wave patterns over a variety of ocean wave and wind conditions. The wave heights varied from 2 m to 5 m, and wind speeds varied from 2 m/s to 25 m/s during the experiment. The surface measurements included four directional wave buoys providing both ocean wave and wind field information.

The radar backscatter is usually modeled by a two-scale Bragg-scattering model. This model means that the backscattered field is not represented by individual infinitesimal scattering sources. However, it can be modeled by the resonant return at a single ocean wave number. The smallest area over which this resonance can occur, called a facet, is small compared with the radar resolution cell size. The gravity wave image formation and distortion is caused by a combination of mechanisms, including tilt modulation, hydrodynamic modulation, velocity bunching, and velocity smearing (azimuth cutoff). The first three of these mechanisms can be described by a linear modulation transfer function over a limited range of ocean and radar conditions. This linearity allows an estimate of the directional wave spectrum from the image spectra in a straightforward manner [e.g., *Vesecky and Stewart*, 1982; *Hasselmann et al.*, 1985]. However, it is now generally agreed that nonlinearities due to the surface motion often complicate the extraction of the directional spectrum [e.g., *Brüning et al.*, 1988].

The SAR measurements of ocean waves are usually in agreement with surface wave measurements when the ocean waves are traveling near the range direction or when other conditions are satisfied, for example, when the ratio of radar range (R) to platform velocity (V) is small. At other times, the SAR-derived directional wave spectrum is distorted with the ocean wave number vector rotated toward the radar range direction. A correction can be applied to these rotated spectra provided that the rotation is not too large. However, a quantitative estimate of the velocity smearing that causes this distortion is required before such a correction can be applied.

Image distortions due to surface motion are separated into two mechanisms, velocity smearing and velocity bunching. Velocity smearing is caused by random radial velocities, sensitive to ocean wavelengths of about 1 m to 10 m, the size of a degraded radar resolution cell. Velocity smearing is typically the most important of the two mechanisms. The azimuth spectral cutoff σ_k is directly related to the scene coherence time of the radar. This cutoff and a model are used to extract the velocity smearing σ_v, which is inversely related to this coherence time. Velocity bunching causes a wavelike pattern and/or distortion in the image, depending on the relative amount of velocity bunching. The bunching shifts the azimuth position of adjacent resolution cells due to the coherent orbital motion of the long-wave advected facets. The velocity bunching over a limited range of ocean and radar parameters is a linear mapping. The orbital acceleration of the long waves is not considered, since it is a second-order effect [*Alpers and Brüning*, 1986].

Several scientists have investigated velocity smearing. *Beal et al.* [1983] reported smearing linearly dependent on the R/V ratio and a square root dependence on $H_{1/3}$. *Tucker* [1985] characterized the smearing in terms of a azimuth low-pass filter, modeled by a Gaussian shape. *Alpers and*

Paper number 91JC00418.
0148-0227/91/91JC-00418$05.00

Brüning [1986] extended this model, giving a surface wind speed dependence under certain conditions, in addition to the R/V and $H_{1/3}$ dependencies. These models all rely on the random motion of radial facet velocities within a radar resolution cell. *Lyzenga et al.* [1985] analyzed waves in water and ice, clearly showing both nonlinear velocity bunching and velocity smearing. Nonlinear velocity bunching causes harmonics in azimuth wave number. Ocean wave harmonics have not been observed in SAR imagery, implying they are always attenuated by the smearing (azimuth spectral cutoff).

In the present work, the two-dimensional intensity wave spectra are averaged in the range coordinate to create one-dimensional azimuth spectra. This processing also includes intensity normalization and a system impulse correction. The one-dimensional spectra are approximated by a Gaussian low-pass filter using a least squares fit to obtain a spectral width σ_k, which is inversely proportional to the velocity smearing, σ_v. A model for the radar-extracted velocity smearing is developed which includes a correction for the radar incidence angle dependence. A first-order model, including the incidence angle correction, is applied to the European Space Agency remote sensing satellite (ERS 1) spaceborne SAR to estimate when it will image ocean wave swell. The relationship between velocity smearing, and ocean surface wind speed is examined.

2. Experiment Description

NORCSEX '88 contained several remote-sensing and in situ instruments assembled to investigate SAR imaging of ocean features including ocean waves. The remote-sensing instruments include the Canadian CV-580 aircraft configured with a C band (f_0 = 5.3 GHz) SAR [*Livingstone et al.*, 1987] and a radar altimeter on board the Geosat spacecraft. The radar altimeter measures spatial variations in wave height and surface wind along the spacecraft ground track every 7 km. The directional wave buoys are spaced about 100 km apart, providing temporal and spatial variations of surface wave and wind field every 3 hours.

The aircraft SAR accumulated data for a total of 28 hours over 6 days between March 11 and March 28, 1988. The radar was configured with vertical transmit and receive polarizations and a seven-look real-time digital processor. Multilooking radars usually sum in intensity. The Canadian radar summed seven looks in amplitude to form each image. These amplitude values are squared during postflight processing to obtain the intensity image. Squaring of the amplitude sum can introduce cross-modulation products that distort the image. The intensity modulation is adequately represented by the amplitude summed imagery on the three days analyzed, since the normalized modulation (the ratio of the rms intensity to the mean intensity) was less than 0.3. Furthermore, workers at the Foundation of Applied Research at the University of Tromsø (FORUT) in Norway have compared one-look (amplitude squared) with seven-look (amplitude squared) image spectra for March 11. They show good agreement with spectral peak and shape between the one- and seven-look results for a number of radar-ocean wave geometries. These results include one-dimensional spectra along the direction the ocean waves were traveling and the associated two-dimensional spectra (H. Johnsen, FORUT, private communication, 1990).

TABLE 1. Aircraft SAR Radar Parameters Used for Spectral Processing

	Nadir Narrow Swath	Wide Swath
Swath width	16.4 km	63 km
Radar resolution* ρ_a (azimuth) × ρ_r (slant range)	6 m × 6 m	10 m × 20 m†
Sample spacing δx	3.89 m	6.22 m
Sample spacing δr	4 m	15.7 m†

*The radar resolution ρ_a is based on seven looks.
†Given is ground range (y).

The aircraft SAR operated in two modes: narrow swath with ground range coverage of 16 km, and wide swath with coverage of 63 km. The multilook radar resolution, given in Table 1, is 6 m in azimuth by 6 m in slant range for the narrow swath and 10 m in azimuth by 20 m in ground range for the wide swath. The radar signals are digitally recorded using 4096 range cells for each mode.

3. Imaging Model

The model used to relate the ocean wave to image spectra is the two-scale Bragg scattering model used in conjunction with velocity-smearing and velocity-bunching models. This model has been described in detail by others [e.g., *Alpers and Rufenach*, 1979; *Rufenach and Alpers*, 1981; *Alpers et al.*, 1981; *Hasselmann et al.*, 1985; *Lyzenga*, 1988].

The model assumes (1) that backscattering can be represented by two-scale Bragg scattering, (2) that backscattering facets are random variables, and (3) that motion contributions are described by a two-scale SAR model. The SAR model is separated into two parts: ocean wavelengths shorter than twice the radar resolution and wavelengths longer than twice the radar resolution. Smearing is caused by random radial velocities of the intermediate-scale waves (wavelengths of about 1–10 m). Bunching is caused by the coherent radial velocities of the long wavelengths, say, peak wavelengths of 100–300 m. The total mean square intensity is the sum of these two mechanisms provided the real aperture (tilt and hydrodynamic) modulation is negligible. The wave number regions in the two-scale SAR model are illustrated in Figure 1*a*. A pictorial illustration of the superposition of velocity bunching and smearing is given in Figure 1*b*. The scattering surface is represented by the rectangular radar cells at A. Velocity bunching is represented by systematic azimuthal shifts to adjacent radar cells at B. Velocity smearing is represented by random motion within a cell in C causing smearing across several cells. Furthermore, we assume that scanning, based on gravity waves traveling near the range direction, distorts the direction in which the waves are traveling [*Rufenach et al.*, this issue]. The maximum directional distortion occurs near the spectral peak, about 10°, with negligible distortion in ocean wavelength.

The two-dimensional intensity spectrum $S_i(k_x, k_y)$ can be represented as the product of three functions; a low-pass filter $|F(k_x)|^2$, a SAR transfer function $|R^{\mathrm{SAR}}(k_x, k_y)|^2$, and the directional wave height spectrum $S_w(k_x, k_y)$. This intensity spectrum is given [e.g., *Lyzenga*, 1988], by

$$S_i(k_x, k_y) = \sigma_0^2 |F(k_x)|^2 |R^{\mathrm{SAR}}(k_x, k_y)|^2 S_w(k_x, k_y) \qquad (1)$$

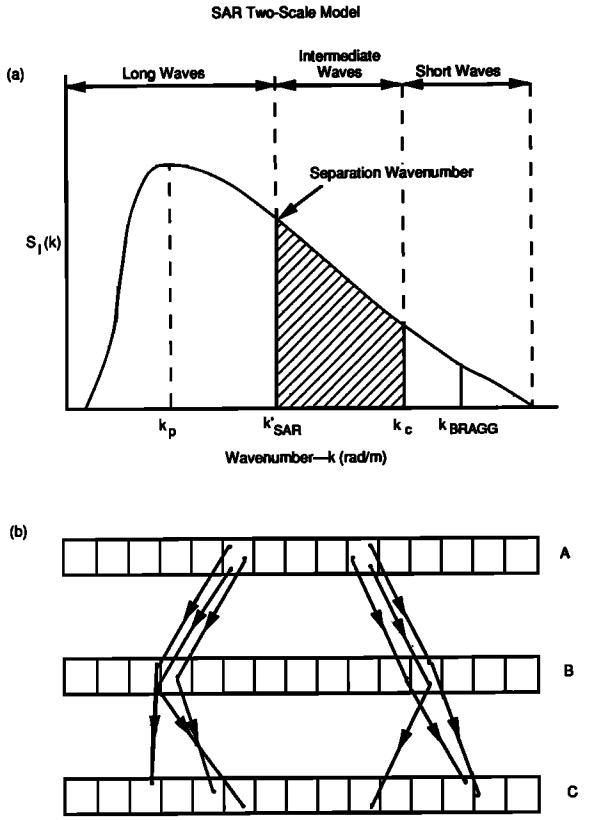

Fig. 1. (*a*) Two-scale SAR model indicating spectral scales for the different wave number regions. For a C band (5.66 cm) radar, $k_p < k'_{SAR} < k_c < k_{BRAGG}$, where k_p is the peak wave number k'_{SAR} is the two-scale separation wave number (π/ρ'_a), k_c is the spectral break point which satisfies the two-scale Bragg conditions, and $k_{BRAGG} = 4\pi \sin(\theta)/0.0566$ m. The hatched area indicates intermediate-scale waves. (*b*) Pictorial illustration of velocity bunching and velocity smearing indicating azimuth shifts caused by radial velocities. The radar-scattering surface is depicted by A, the shifts due to velocity bunching by B, and the random shifts within a resolution cell (smearing) by C, after *Tucker* [1985].

where σ_0 is the radar cross section per unit area, k_x is the wave number in the platform velocity direction (azimuth direction), k_y is the wave number in the ground range direction, and $|F(k_x)|^2$ is the velocity-smearing low-pass filter given by

$$|F(k_x)|^2 = \exp(-k_x^2/\sigma_k^2) \tag{2}$$

where $\sigma_k = 1/\sigma_x(\theta) = 1/(R/V)\sigma_v(\theta)$ is the rms spectral width, $\sigma_x(\theta)$ is the rms spatial width, R is the slant range distance to the surface, and V is the platform velocity. The velocity smearing, $\sigma_v(\theta)$, is the rms radial facet velocity within a degraded resolution cell, given by

$$(\sigma_v(\theta))^2 = \int_0^{2\pi} \int_{\Omega'_{SAR}}^{\infty} G^2(\theta, \phi) S_w(\omega, \phi) \omega^2 \, d\omega \, d\phi \tag{3}$$

where $\Omega'_{SAR} = (gk'_{SAR})^{1/2}$ is the separation frequency of the two-scale SAR model, k'_{SAR} is the corresponding wave number separation, the prime signifies a degraded resolution parameter, ϕ is the azimuth angle with respect to the k_x axis, $\cos\phi = k_x/k$, θ is the radar incidence angle, and $G^2(\theta, \phi)$ is the geometric factor for the long ocean waves, given by

$$G^2(\theta, \phi) = \cos^2\theta + \sin^2\theta \sin^2\phi \tag{4}$$

The modulation transfer function (MTF) is $|R^{SAR}(k_x, k_y)|^2$, where $R^{SAR} = R^{SAR} + R^B$, R^{RAR} is the modulation measured by a real aperture radar, and R^B is the modulation caused by velocity bunching as measured by SAR.

The radar samples temporal frequencies along the x direction, $\omega_x = Vk_x$, where the platform velocity is larger than other velocities of ocean surface motion. However, this does not mean that surface motions can be ignored. The one-dimensional intensity spectrum in the x direction is given by

$$S_i(k_x) = \int_{-\infty}^{\infty} S_i(k_x, k_r) \, dk_r \tag{5}$$

where the slant range (k_r) integration is orthogonal to the k_x direction. Equation (5) is equivalent to the averaging of the two-dimensional spectra accomplished during processing to obtain a one-dimensional spectrum. A one-dimensional wave height spectrum and modulation transfer function can be defined similarly.

We assume that the radar cross section is constant or, equivalently, that the modulation portion of R^{RAR} is negligibly small in the k_x direction for a given k_r. This is true provided that $\phi_0 \approx 90°$, where ϕ_0 is the peak wave direction defined with respect to k_x. Indeed, the real modulation is maximum in the range direction and minimum in the azimuth direction [e.g., *Alpers et al.*, 1981; *Brüning et al.*, 1988]. Substituting (1) into (5), one obtains

$$|F(k_x)|^2 = S_i(k_x)/[\sigma_0^2 |R^B(k_x)|^2 S_w(k_x)] \tag{6}$$

where $|R^{SAR}(k_x)|^2 \approx |R^B(k_x)|^2$ is the velocity-bunching transfer function,

$$|R^B(k_x)|^2 = (R/V)^2 g k_x^3 \bar{G}_i^2(\theta) \tag{7a}$$

and

$$\bar{G}_i^2(\theta) = \int_{-\infty}^{\infty} (\cos^2\theta + k_y^2/k^2 \sin^2\theta) \, dk_y \tag{7b}$$

where $\sin^2\phi = k_y^2/k^2$, $k^2 = k_x^2 + k_y^2$ and we use the ground range wave number k_y in (7*b*) rather than the slant range wave number k_r. Equation (7*b*) is approximately independent of k_x on the basis of the dominant waves traveling near the range direction, $\phi_0 \approx 90°$; i.e., $G^2(\theta, \phi) \approx \cos^2\theta + \sin^2\theta = 1$. This dependence is discussed in more detail below. Equation (7*a*) is valid for linear velocity bunching where g is the acceleration of gravity.

An analytic form for the intrinsic velocity smearing σ_v in terms of the radar extracted velocity smearing $\sigma_v(\theta)$ can be calculated, provided that an analytical form for the intermediate scale directional wave spectrum is available. The directional wave spectrum is assumed,

$$S_w(\omega, \phi) = S_w(\omega) D(\phi, \phi_0) \tag{8}$$

where the directional spreading function D is independent of ω. This approximation is reasonable over the limited frequency range of intermediate-scale waves. The extracted velocity smearing $\sigma_v(\theta)$ is then given by a product of the intermediate-scale geometric factor $\bar{G}_i(\theta, \phi_0)$ and the velocity smearing σ_v,

$$\sigma_v(\theta) = \bar{G}_i(\theta, \phi_0)\sigma_v \tag{9}$$

where σ_v is independent of θ and ϕ_0, and σ_v and $\sigma_v(\theta)$ are independent of R/V. The geometric factor $G(\theta, \phi)$ averaged over all azimuth angles is

$$\bar{G}_i^2(\theta, \phi_0) = \int_0^{2\pi} G^2(\theta, \phi)D(\phi, \phi_0)\, d\phi \tag{10}$$

and the velocity smearing σ_v is expressed as

$$\sigma_v^2 = \int_{\Omega'_{SAR}}^{\infty} S_w(\omega)\omega^2\, d\omega \tag{11}$$

where the prime indicates the degraded resolution, usually defined in terms of degraded azimuth resolution ρ'_a which is inversely proportional to Ω'_{SAR}. A spectral form for $S_w(\omega)$ is assumed [*Donelan et al.*, 1985; *Banner*, 1990],

$$S_w(\omega) = \alpha(U)g^2\omega^{-5} \tag{12}$$

$$D(\phi, \phi_0) = f(s)\cos^{2s}((\phi - \phi_0)/2) \tag{13}$$

where $\alpha(U) \sim U$, $\alpha \approx 0.01$ for a fully developed sea, U is the surface wind speed, g is the acceleration of gravity, and $f(s)$ is a normalizing factor such that the integration of the angular wave spectrum is 1. Substituting (13) into (10) for $s = 0$ gives

$$\bar{G}_i^2(\theta) = \cos^2\theta + 0.5\sin^2\theta \tag{14}$$

where $D(\phi, \phi_0) = 1/2\pi$ is an isotropic directional distribution. In comparison, $s = 2$ gives

$$\bar{G}_i^2(\theta, \phi_0) = \cos^2\theta + 0.5\sin^2\theta\sin^2\phi_0 - 0.08333\sin^2\theta\cos 2\phi_0 \tag{15}$$

where $D(\phi, \phi_0) = (4/3\pi)\cos^4[(\phi - \phi_0)/2]$. In both of these cases ($s = 0$, 2) the radar-extracted velocity smearing is a function of incidence angle, and for the case $s = 2$ the maximum smearing occurs when the intermediate waves are traveling in the range direction, $\phi_0 = 90°$. Indeed, the velocity smearing is dependent on the direction the intermediate waves are traveling provided that the waves have a preferred direction of travel as illustrated in Figure 2. Substituting (12) into (11) gives

$$\sigma_v \approx 1.25\alpha_i(U)^{1/2}(\rho'_a)^{1/2} \tag{16}$$

where $\alpha_i(U)$ is a intermediate-scale parameter increasing with wind speed based on an equilibrium spectrum [*Banner*, 1990]. However, at a sufficiently high wind speed, the spectrum saturates; then $\alpha_i = 0.0081$ and $\sigma_v \approx 0.112(\rho'_a)^{1/2}$. Equation (16) is consistent with *Alpers and Brüning* [1986] when $\Omega_p < \Omega'_{SAR}$, where Ω_p is the dominant longwave frequency. We consider this as the relevant approximation for essentially all open ocean SAR measurements. Indeed, a fetch of a few kilometers under light wind, about 6 m/s, is sufficient to generate waves with wavelengths of intermediate scale, about 1 to 10 m. Therefore, $\Omega_p < \Omega'_{SAR}$ is essentially always satisfied in the open ocean. The growth rate can be calculated using the fetch-limited relationship with $u_* \approx U_{10}/25$ [e.g., *Phillips*, 1977].

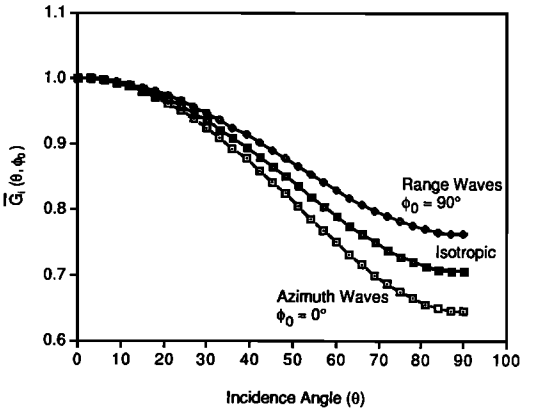

Fig. 2. Geometric factor $\bar{G}_i(\theta, \phi_0)$ for intermediate-scale gravity waves based on two different directional distributions: (1) isotropic, $D(\theta) = 1/2\pi$, corresponding to the middle curve, and (2) $D(\theta, \phi) = (4/3\pi)\cos^4[(\phi - \phi_0)/2]$, corresponds to the top curve ($\phi_0 = 90°$) and the bottom curve ($\phi_0 = 0°$).

A two-dimensional rectangular wave number spectrum for the long ocean waves, $S_w(k_x, k_y)$, is appropriate for SAR in order to estimate $|F(k_x)|^2$ from equation (6). We select, for the moment, a spectral form

$$S_w(k_x, k_y) = C_k[1 + C_x^2k_x^2 + C_y^2k_y^2]^{-\delta/2} \tag{17}$$

to illustrate the decrease by 1 of δ from a two-dimensional spectrum to a one-dimensional spectrum. The asymptotic wave number index corresponds to a two-dimensional Phillips spectrum when $\delta = 4$, where δ is the power law index. Following (5), we obtain

$$S_w(k_x) = \int_{-\infty}^{\infty} S_w(k_x, k_y)\, dk_y \tag{18}$$

substituting (17) into (18) and assuming that C_y varies slowly with the integration variable k_y,

$$S_w(k_x) = C_k[1 + C_x^2k_x^2]^{-(\delta - 1)/2} \tag{19}$$

Thus the asymptotic power law index for the one-dimensional spectrum is $\delta - 1$ instead of δ, where $\delta - 1 = 3$ for a one-dimensional Phillips asymptotic spectrum as given in (19).

On the basis of dimensional analysis, the one-dimensional spectral density decreases with increasing wave number as k_x^{-3},

$$S_w(k_x) = C_xk_x^{-3} \tag{20}$$

Substituting (20) into (6) results in a filter width $\sigma_k = \sigma_{ik}$ (where σ_{ik} is one-dimensional intensity width), since $|R^B(k_x)|^2S_w(k_x)$ = constant. The measured one-dimensional wave number value is $\delta - 1 \approx 3$, consistent with (20) and *Schule et al.* [1971].

Equations (6) and (14) are used in the next section to estimate velocity smearing σ_v, using the measured azimuth intensity spectrum $S_i(k_x)$, where $\sigma_k = \sigma_{ik}$ on the basis of $S_w(k_x) \propto k_x^{-3}$.

4. DATA ANALYSIS

The measurements were selected such that the observed peak range angle was always less than about 5°. That is, the intrinsic peak range angle $|\phi_0 - 90°|$ is less than about 15° on the basis of a maximum scanning distortion of 10°. However, this directional (range angle) distortion is much smaller than 10° for the analysis in the present work, since the relevant ocean wavelengths are much shorter than the peak values. This 5° criterion lessens the nonlinearity of velocity bunching. The importance of minimizing the nonlinearity of velocity bunching is not known. However, *Lyzenga* [1988] has shown that smearing and velocity bunching are separable even for nonlinear velocity bunching. This suggests that the filter width can be extracted from the imagery over a wide range of radar configurations and sea conditions.

The subimage spectra were calculated using 512 × 512 samples in the narrow swath mode (resolution) δk_x = 0.0032 rad/m) and 512 × 1024 samples in the wide swath mode (δk_x = 0.00197 rad/m). Three subimages were analyzed at near, mid, and far ranges for each processing area. This allowed a check on the internal consistency of the rms smearing. This consistency check is possible because σ_v should not change with R/V ratio. The one-dimensional azimuth spectra, $S_i(k_x)$, were calculated by averaging 64 pixels (δk_r = 0.00153 rad/m) in the slant range coordinate centered on the peak wave number. The spatial sampling size is given in Table 1.

The azimuth spectra were obtained by first, normalizing the image intensity by calculating its zero mean intensity variation divided by its mean, $(I - \langle I\rangle)/\langle I\rangle$; second, range averaging the spectral values; and third, correcting for the impulse response of the radar using a quadratic approximation to the high k_x values. Figure 3 illustrates the method of analysis. The analysis method was applied to the wave imagery acquired on March 14, 17, and 20 for gravity waves traveling near the range direction. An example of the one-dimensional spectra taken on March 14, pass 4, is shown in Figure 4*a*. The spectra are plotted on semilog coordinates for the near (R/V = 113.4) and mid (R/V = 196.4) areas of the swath. The width of these azimuth spectra were estimated by a least squares fit to a Gaussian spectral shape as shown in Figure 4*b*. Equations (21) and (14) were used to estimate the velocity smearing σ_v from the spectral width σ_k.

The measured azimuth spectra $S_i(k_x)$ were divided by $|R_B(k_x)|^2 S_w(k_x)$ to extract estimates of the low-pass filter $|F(k_x)|^2$ as a function of k_x (see equations (2) and (6)). Two forms of $S_w(k_x)$ were assumed, k_x^{-3} and the Pierson-Moskowitz spectrum [*Pierson and Moskowitz*, 1964] with a low-wave-number cutoff designated as k_0. We found that σ_v and $|F(k_x)|^2$ were sensitive to this cutoff for some of the data analyzed, causing scatter in σ_v as a function of R/V and lower correlation coefficients. Furthermore, we found it difficult to determine whether this low-wave-number scatter

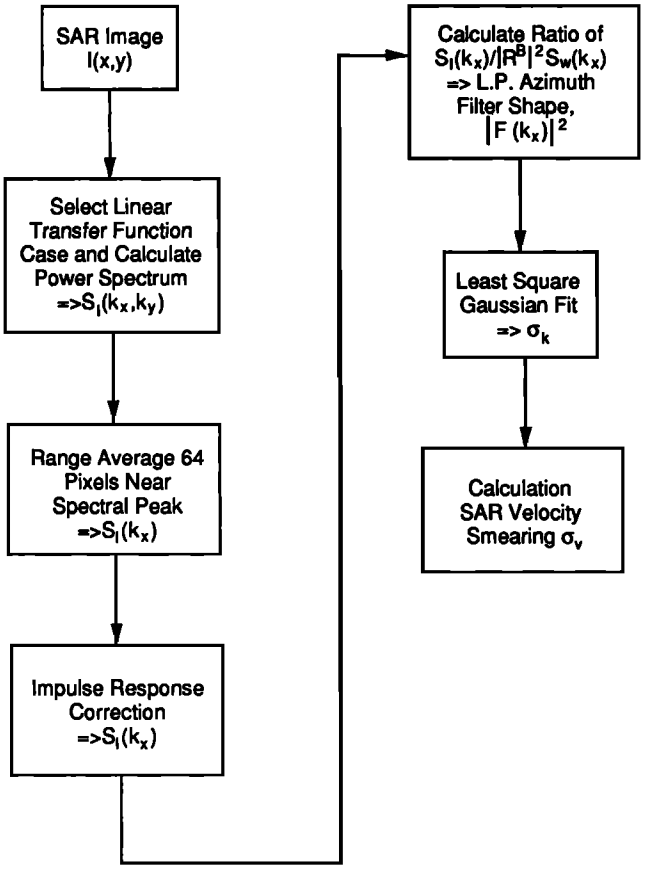

Fig. 3. Block diagram of spectral analysis method used to estimate velocity smearing σ_v.

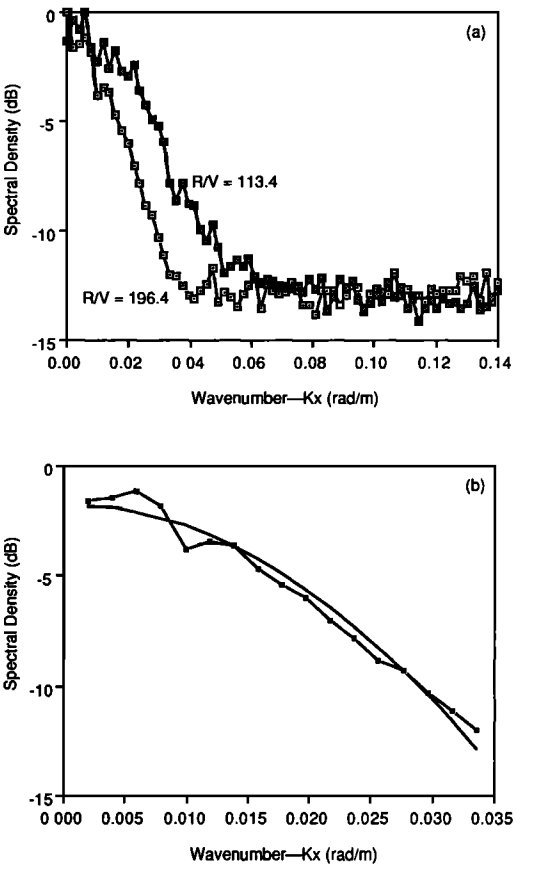

Fig. 4. (*a*) Example of azimuth spectral density using (bottom) R/V = 196.4 and (top) R/V = 113.4 for March 14, pass 4. The S/C ratio is about 13 dB for both spectra, where S is the spectral density of the signal and C is the spectral density of the clutter. (*b*) Gaussian least squares fit (solid line) to the azimuth spectral density, R/V = 196.4 (midrange) example, in Figure 4*a*. The filter width is σ_k = 0.0217 ± 0.0004 rad/m, and the correlation coefficient is R = 0.98.

TABLE 2. Sample σ_v Results Using March 20, Pass 1, Measurements

Range	R/V	θ, deg	σ_k, rad/m	rms Error	r*	$\sigma_v(\theta)$, m/s	σ_v, m/s	S/C, dB	$\bar{G}_i(\theta)$†
Far	155.3	71.9	0.0122	±0.0007	0.93	0.528	0.714	15	0.74
Mid	116.4	65.4	0.0157	±0.0009	0.904	0.547	0.714	19	0.77
Near	89.1	56.9	0.0217	±0.0034	0.982	0.534	0.662	20	0.81

*Correlation coefficient.
†$\bar{G}_i^2(\theta) = \cos^2\theta + 0.5\sin^2\theta$.

in $|F(k_x)|^2$ was caused by changes in k_0 or ϕ_0. We therefore select k_x^{-3} as the wave number variation in the present work. Each individual extracted $|F(k_x)|^2$ was examined for deviation from the low-pass Gaussian variation by plotting the measurements and the fit on the same plot (see Figure 4*b*). The first three or four k_x values were ignored in the least squares fit if significant deviation was observed. That is, the difference between the measurements and fit at these first few points is large compared with the higher values of k_x. We feel that this procedure results in realistic first-order estimates of the velocity smearing based on

$$\sigma_v = 1/(R/V\sigma_k\bar{G}_i(\theta)) \tag{21}$$

provided the measurements are not near atmospheric fronts and the extracted σ_v are independent of R/V. Equation (21) is obtained by substituting (9) into (2). A discussion of these conditions and their associated errors are given below.

Several factors can contribute to errors in the estimate of σ_v. First, the accuracy of the least squares fit is dependent on $k_{\min}$, where $k_{\min}$ is the break point between the spectral density of the signal (S) and the density of the clutter (C) background, or speckle. An increase of a few sampling wave number widths, $\delta k_x = 2\pi/(512\ \delta x)$, in $k_{\min}$ can underestimate the smearing by up to about 5%, whereas a decrease in wave number of a few sampling widths had little or no effect provided the signal-to-clutter ratio is $S/C > 10$ dB. Second, the regression fit varies with a correlation coefficient from about 0.8 to 0.99, with 1.0 being a perfect fit. The goodness of the fit describes how well the low-pass filter approximates a Gaussian shape, which is an indicator of the model validity. Third, the accuracy of the imaging model, including the two-scale Bragg-scattering assumptions, can cause errors, especially near atmospheric wind fronts where the winds are highly variable and at times of high winds and waves. Indeed, the intrinsic lifetime of the Bragg short waves may bias the smearing. Fourth, the validity of the one-dimensional wave height spectral form including the asymptotic power law index $\delta - 1$ and the low-wave-number cutoff are also possible sources of error. We varied the power law index δ as a sensitivity check for a number of subimages. Indeed, the directional spreading function D is dependent on k near the peak wave number, but the exact form is not well known [*Banner*, 1990]. Typical errors were 5% for $\delta - 1 = 3 \pm 0.5$. We do not expect the direction spreading near the peak to cause errors much larger than 5%. We estimate the total error to be less than 10% provided that the measurements are not near wind frontal boundaries and/or the smearing σ_v does not change more than 10% with R/V.

Three subimages processed on March 20 illustrate the method. They show essentially a constant value of σ_v for the three R/V ratios, $\sigma_v \approx 0.7$ m/s (see Table 2). The σ_v estimates assume an isotropic directional function given by (14). The internal consistency for the constancy of σ_v with R/V provides confidence in the method. However, some of the other subimages processed show a decrease in σ_v with increasing R/V of up to about 15% (see, for example, Figure 10). The average value of the near and mid range was used when this decrease was present.

The reliability of this analysis method can be investigated by comparison with another independent method. *Johnsen et al.*, [this issue] used another method to estimate σ_v from the March 11 imagery. However, it requires two R/V ratios at the same subimage processing area, which unfortunately requires two aircraft flights along the same path at two altitudes. These two methods gave comparable results.

The σ_v values are also compared with (16) using the results from March 20. As given in Table 3, σ_v varies from 0.45 to 0.7 m/s based on (6) while $\sigma_v \approx 0.3$ m/s based on (16) with $\rho_a' = \rho_a \approx 6$ m. One possible explanation why (16) underestimates the measurements is that the radar resolution should include the effects of ocean wave motion. The appropriate resolution is then the degraded resolution given by $(\Omega_{SAR}')^2 = gk_{SAR}' = \pi/\rho_a'$ and $\rho_a' > 6$ m where the prime

TABLE 3. SAR-Derived Velocity Smearing σ_v

Date	Pass	σ_v, m/s	Incidence Angle θ,* deg	$\bar{G}_i(\theta)$†	$H_{1/3}$, m	U, m/s	$\rho_a \times \rho_r$, m × m
March 14	4	0.37	80	0.7	1.9‡	2.0‡	10 × 20
March 17	4	0.4	70	0.7	2.2§	5.3§	10 × 20
March 20	1	0.45–0.7	60	0.8	3.6–4.69	6–18	6 × 6

*Approximate value.
†$\bar{G}_i^2(\theta)\cos^2\theta + 0.5\sin^2\theta$.
‡Values calculated using buoy 2 data at 1645 UT within about 20 km and 10 min of the SAR measurement.
§Values interpolated between buoy 1 at 08:45 and 11:45 GMT within about 20 km of the SAR measurement.

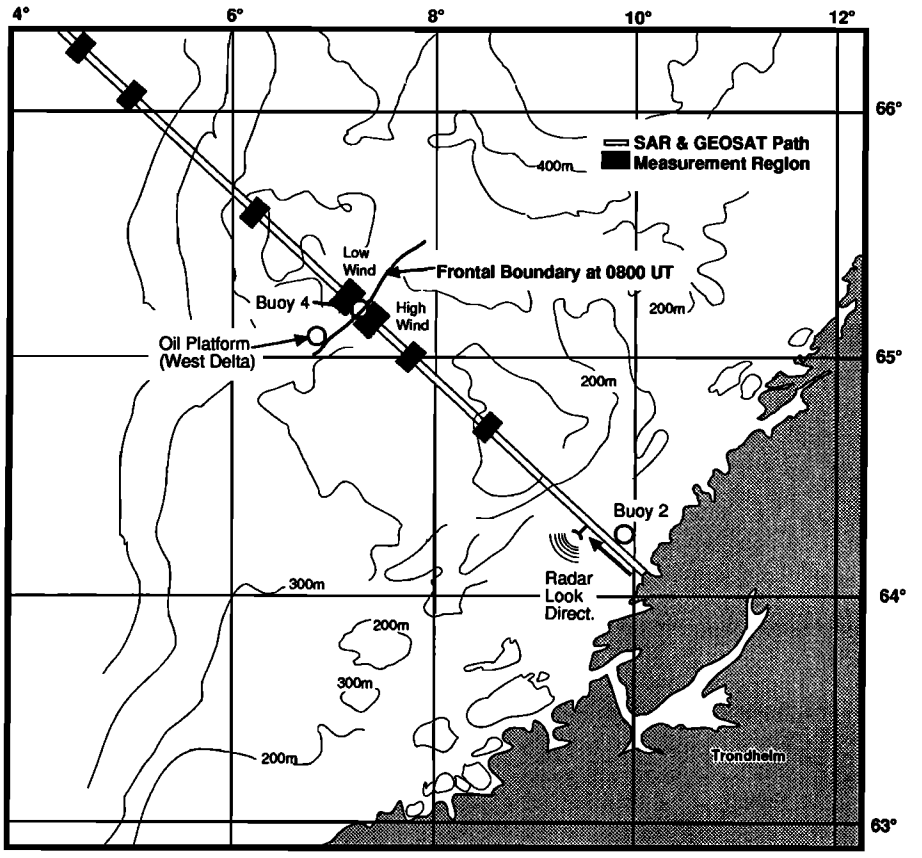

Fig. 5. Plan view of aircraft SAR and Geosat altimeter coaligned paths on March 20, 1988, off the coast of Norway. The locations of pitch and roll buoys 1 and 4, oil platform "West Delta," and the atmospheric frontal boundary are indicated. The arrow near buoy 2 indicates the aircraft flight direction for pass 1. The aircraft flight was in the opposite direction for pass 2 about 1 hour later.

indicates degraded resolution rather than the stationary resolution. This interpretation means that (11) is a nonlinear integral equation, since $\sigma_v(\Omega'_{SAR})$ depends on the lower limit of integration, Ω'_{SAR}. Indeed, both the smearing and bunching can degrade the resolution. This interpretation appears reasonable, since the total mean square intensity is the sum of the smearing and bunching if the tilt and hydrodynamic modulations are ignored. Therefore if Ω'_{SAR} decreases (ρ'_a increases), the smearing increases and the bunching modulation decreases provided that the spectral density near Ω'_{SAR} does not change much.

Smearing measurements were analyzed for 3 days in March 1988. The σ_v estimates for these three days are given in Table 3. The radar was operated in the wide swath mode on March 14 and 17, and the narrow swath mode on March 20 as indicated by the radar resolution in Table 3. The wave heights and surface winds varied from 2 to 4.7 m and 2 to 18 m/s during the 3 days selected for measurement. The velocity smearing σ_v varied from 0.4 to 0.7 m/s for these 3 days. This quantitative result is an important input to models of wave image distortion. Any inferred wind speed dependence of σ_v estimates within ±8 km of the frontal boundary are suspect, as is discussed below.

5. Geosat Underflight Measurements

The aircraft SAR was flown along the Geosat spacecraft ground track and over two directional wave buoys aligned along the path on March 20, as illustrated in Figure 5. The Geosat radar altimeter measured the significant wave height and the nadir (vertical incidence) radar cross section every 7 km. The cross section has been used to estimate the surface wind speed [e.g., *Brown*, 1979]. Two directional wave buoys were located near each end of the SAR pass. These buoys measured winds and waves, while an oil platform measured winds. All of the ground-based measurements were acquired at 3-hour intervals.

The smearing was analyzed at three areas coaligned along the aircraft and spacecraft paths, equally spaced about every 50 km south from the frontal boundary, six areas within 8 km of the boundary, and four equally spaced areas north from the boundary. The variation of σ_v at these locations as a function of geographic latitude is shown in Figure 6*a* for pass 1, where the aircraft was flying northwest. The σ_v values along the path show values near 0.53 m/s, followed by scatter in the values near the boundary then followed by an increasing σ_v out to a maximum ($\sigma_v \approx 0.6$ m/s) near 65.7°N, with decreasing σ_v for the remaining values. The aircraft also flew (pass 2) about one hour later in the opposite direction, with a slightly shorter path so that measurements at the end points in pass 1 were not available for pass 2. The results of the extracted σ_v for pass 2 are similar to pass 1 as given in Figure 6*b*. The large scatter in σ_v estimates near the atmospheric frontal boundary as discussed in the next section.

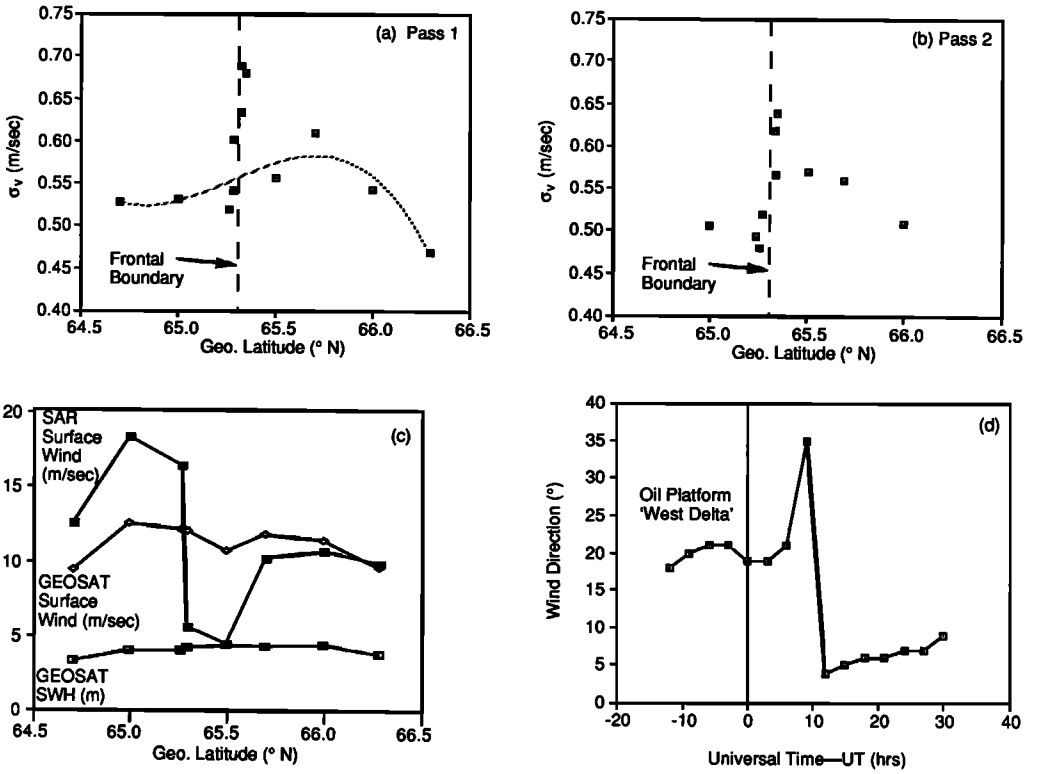

Fig. 6. (*a*) Variation of σ_v with distance along the SAR aircraft path on March 20, pass 1. The dotted line is a polynomial fit to the estimates of σ_v neglecting the six values within ±8 km of the boundary. The interval between data values is about 50 km along the aircraft path for points away from the boundary. (*b*) Variation of σ_v with distance along the SAR aircraft path on March 20, pass 2. The aircraft was flying in the opposite direction of pass 1 about 1 hour after pass 1 and the Geosat overflight. The six values within ±8 km of the boundary show scatter similar to that in Figure 6*a*. The movement of the frontal boundary during this 1-hour period is ignored for this comparison. (*c*) Significant wave height and surface wind speed extracted from measurements along the SAR path using the Geosat altimeter and aircraft C band SAR. (*d*) Wind direction measurements at oil platform "West Delta" taken at 3-hour intervals. The axis is given in hours relative to 0000 UT on March 20, 1988. The frontal boundary traversed the oil platform near 0900 UT.

The variation of $H_{1/3}$ and surface wind speed along the SAR path is shown in Figure 6*c*. These values were extracted from the Geosat altimeter and SAR cross section measurements. The SAR wind results assumed a wind dependence given by *Keller et al.* [1989], namely, a power law index of 1.5. The buoy and the altimeter winds south of the boundary were used to calibrate the wind speed from the relative cross section measurements of the SAR. Furthermore, it was assumed that the wind direction did not change more than 20° near the frontal boundary except at the boundary. This is considered reasonable on the basis of the oil platform measurements of the wind as shown in Figures 6*d* and 11. The wind direction measurements from buoy 4 are suspect because of the large scatter in the direction, greater than 100° over 3-hour intervals.

The large discrepancy between the Geosat and SAR extracted wind speed is unexpected. The half-width of the low wind region along the front is about 40 km based on the SAR cross section. The antenna footprint for Geosat is of the order of 10 km; therefore it should have detected the SAR-extracted large decrease in wind speed provided that the atmospheric attenuation or rain across the frontal boundary were not biasing the measurement.

We consider the three measurement areas spaced 50 km apart southeast of the front to investigate the variation of σ_v

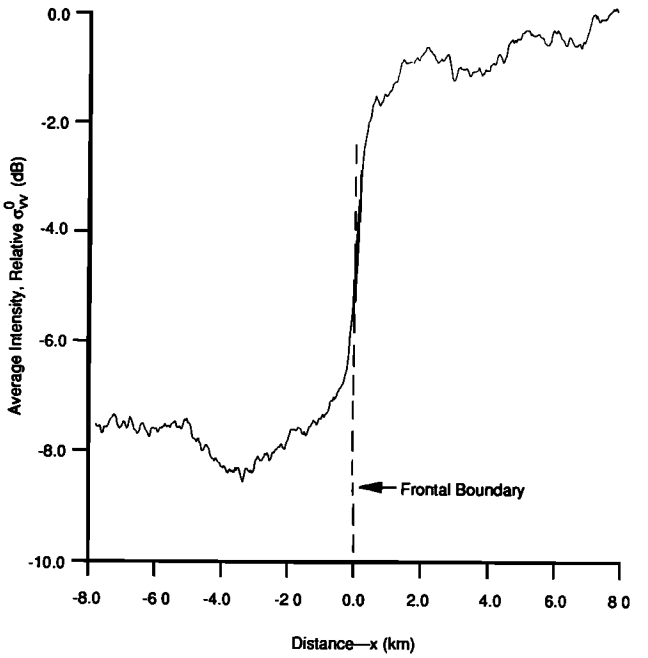

Fig. 7. Variation of mean intensity (SAR cross section) across the atmospheric frontal boundary on March 20, 1988. The boundary signature is a steplike increase in intensity with wind speed.

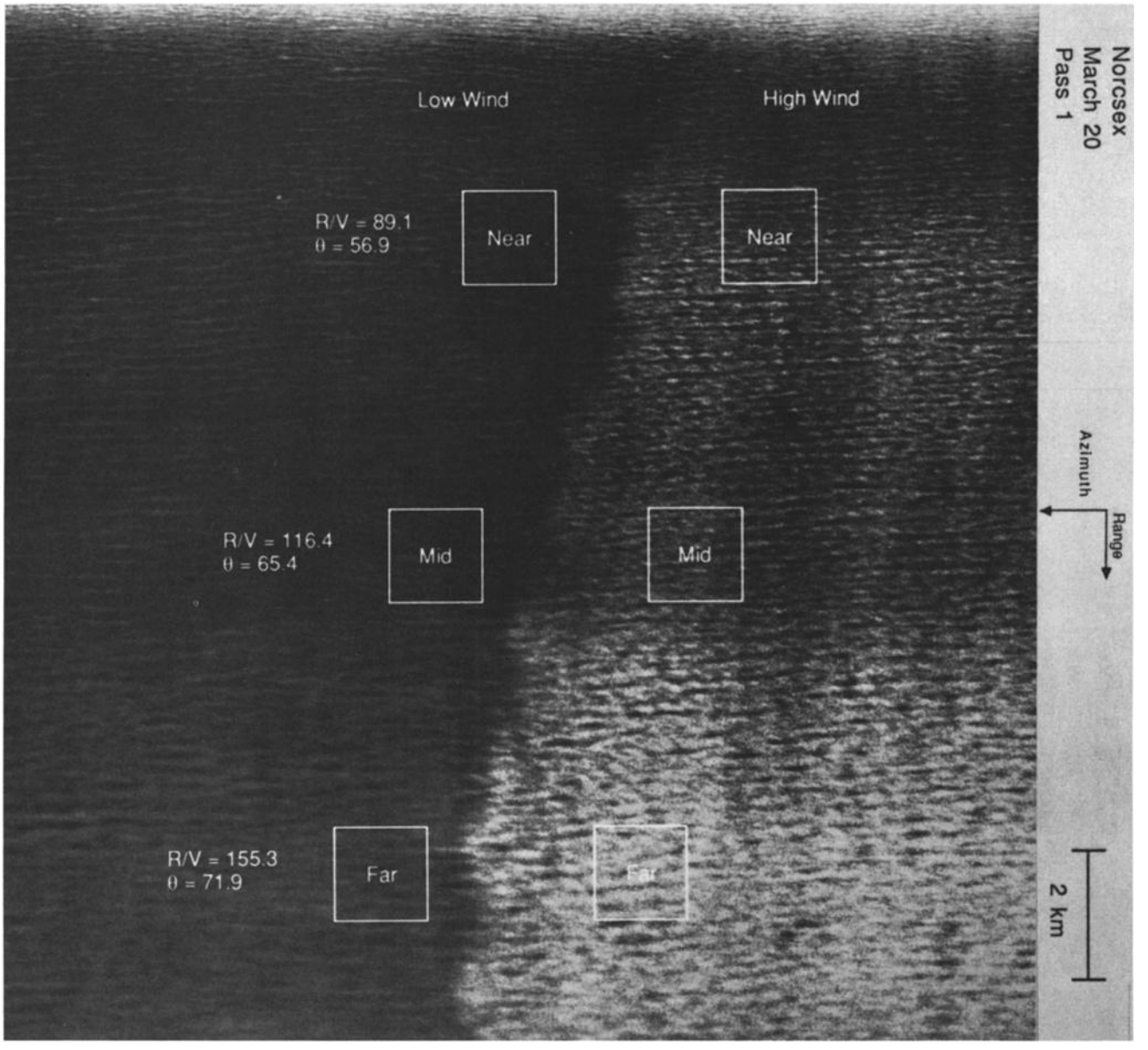

Fig. 8. Synthetic aperture radar image at the atmospheric front of March 20, 1988, off the coast of Norway. The steplike increase in the intensity background across the boundary as shown in Figure 7 corresponds to the bright-dark boundary in the image. The three rectangular areas on each side of the front indicate the approximate locations of the subimages used in the analysis. These areas correspond to R/V = 89.1, 116.4, and 155.3 and θ = 56.9°, 65.4°, and 71.9°.

with significant wave height $H_{1/3}$. The three values of σ_v are nearly constant for $H_{1/3}$ varying from 3.6 m to 4.3 m. The limited range of these measurements are insufficient to establish any dependence or lack thereof on $H_{1/3}$. Additional smearing measurements are needed using coaligned aircraft SARs and spacecraft altimeters to investigate the smearing variation with wave height.

6. Atmospheric Front Measurements

Atmospheric fronts are easily detected as boundary signatures between bright and dark regions of the two-dimensional backscattered intensity. A steplike increase in intensity with wind speed on March 20 caused a sharp bright-dark boundary in the imagery as illustrated in Figure 7. Therefore fronts can be easily located in the imagery, and hence the intensity modulation can be analyzed at areas of interest near frontal boundaries. Velocity smearing values were calculated at two atmospheric fronts (March 17 and March 20). The March 17 subimage spectra provided low signal-to-clutter ratios (~5 dB), and σ_v could not be calculated at the same R/V ratios across the front on account of the front boundary configuration. The March 20 front did not have either of these problems. The S/C ratios varied from 13 to 20 dB and σ_v values were calculated at the same R/V ratios.

The smearing was calculated at three subimages, rectangular areas, on each side of the front on March 20. The gravity wave pattern was visible on both sides of the front

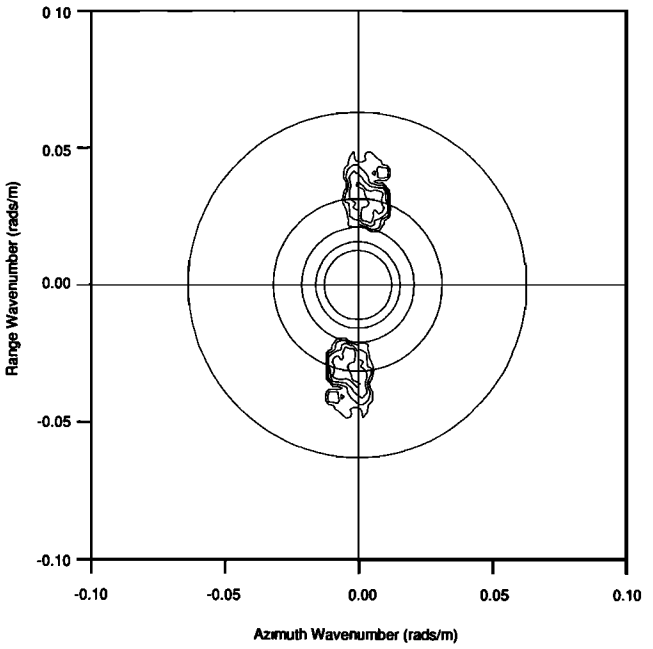

Fig. 9. Intensity spectrum of the image in Figure 7 for R/V = 89.1 at the low-wind side of the front. The circles represent wavelengths from 100 to 500 m in 100-m intervals; the intensity contours are 2 dB intervals.

with waves traveling near the range direction as illustrated in Figure 8. The two-dimensional image spectral peaks across the front are similar at all six sub-images; i.e., no change in direction across the front. A spectral example is given in Figure 9 with a peak wavelength of about 200 m at R/V = 89.1, the near-range case. These spectra yield larger smearing on the low-wind side of the front for all three R/V ratios as shown in Figure 10. The increase in σ_v from about 0.53 m/s on the high-wind side to about 0.7 m/s on the low-wind side over a few kilometers perpendicular to the frontal boundary is unexpected, since equation (16) and *Alpers and Brüning* [1986] both show larger smearing with increasing wind speed. This inverse relationship with wind speed occurs only at the boundary. The SAR-extracted smearing at the boundary is suspect, while smearing away from the boundary are considered reliable (see Figure 6 and section 8).

The growth and dissipation rates associated with the long gravity waves (about 100 m to 300 m) are too long for a significant change over a few kilometers provided that the wind direction is not parallel to the boundary. However, the intermediate-scale waves, with wavelengths of about 1 to 10 m, can change over this distance, as is discussed in section 3. Therefore the long gravity waves cannot change within a few kilometers of the frontal boundary. This suggests that velocity smearing is caused by the intermediate-scale waves provided that the same scattering mechanism dominates on both sides of the frontal boundary.

The surface wind changed from about 6 m/s to about 12 m/s across the boundary based on the SAR, and buoy 4 measurements (see Figure 11). The large gradients in wind speed are inferred from the SAR measurements. The SAR cross section changed about 7 dB in a few kilometers. This change can be caused by two effects: a wind speed change and/or upwind-crosswind directional changes. The maximum differential cross-section change on average is about 3 dB based on the directional wind changes, upwind-crosswind [*Feindt et al.*, 1986]. However, at the boundary the direction changes from about 35° to 5° in a 3-hour interval, see Figure 6*d* about 0.1° in geographic latitude (≈ 15 km) based on a boundary speed of 5 km/h. Therefore we estimate that the surface wind changed from 6 m/s to 12 m/s in a few kilometers at the boundary. The wind speed decrease from near 20 m/s to 5 m/s from 0600 UT to 0900 UT is consistent with the SAR cross-section changes but inconsistent with the Geosat measurements.

We do not understand the increase in smearing σ_v on the low-wind side of the boundary of March 20 pass 1, which is just opposite the variation expected: increasing wind speeds are expected to increase the spectral density at intermediate-scale waves, causing larger random radial velocities, and larger velocity smearing (equation (16)). The σ_v extracted estimates near the front boundary are suspect because the significant scatter cannot be explained by the smearing model used in the present work or by the results of *Alpers and Brüning* [1986]. Additional measurements across fronts are needed to better understand these unexpected changes. Four possible explanations are offered: (1) two intermediate scale wave systems may be present on the low-wind side, which is possible since the dissipation rate of the intermediate waves is typically longer than the growth rate, (2) non-Bragg scattering including specular point and wedge scattering caused by the turbulence near the boundary could be significant, (3) the assumed spectral form for the intermediate scale portion of $S_w(\omega, \phi)$ may not be valid across the fronts where waves are generated and dissipated, and (4) Bragg-scattering waves may be sensitive to the radar geometry and ocean wind and wave conditions including the intrinsic lifetime of the short waves.

7. Minimum Wavelength Model With Application to ERS 1 SAR

One of the primary goals of the NORCSEX '88 experiment was to determine when and under what conditions ocean surface waves can be detected by C band SAR. These results could then be applied to the SAR scheduled for launch on the ERS 1 spacecraft. We use the velocity-smearing model developed in section 3 with the available aircraft SAR smearing results as a first estimate of gravity wave detect-

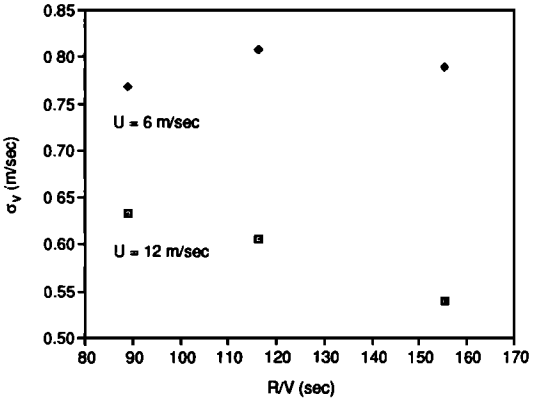

Fig. 10. Variation of σ_v with R/V ratio on both sides of the atmospheric front of March 20, 1988.

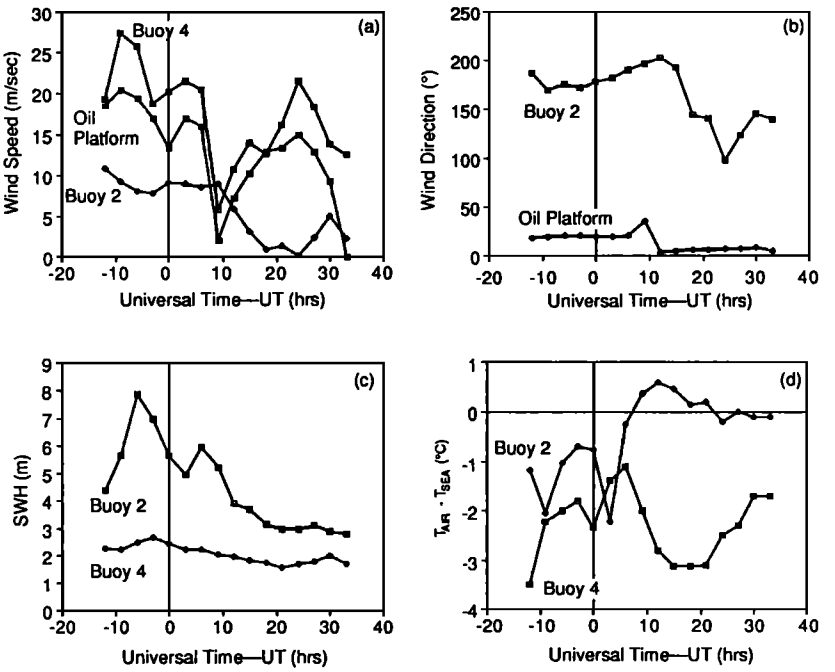

Fig. 11. Directional wave buoy data at buoys 2 and 4 and at oil platform "West Delta," taken at 3-hour intervals. The horizontal axis gives the time of measurement relative to 0000 UT on March 20, 1988. Buoy 4 measurements were taken before and after frontal boundary passage near 0900 UT. The wind measurement height is about 15 m for the oil platform and 3.7 m for buoys 2 and 4. The wind measurements at buoy 4 are suspect.

ability by ERS 1. A correction to the radar sensed smearing is required to apply aircraft measurements to spacecraft incidence angles (see Figure 2). We use measured σ_v values to estimate the azimuth cutoff or, equivalently, the minimum detectable azimuth wavelength, $(L_{\min})_x$; i.e., shorter wavelengths will not be detected. Following *Lyzenga* [1986], $(k_{\min})_x = 2\pi/(L_{\min})_x = 2\sigma_k$, and using equations (9) and (14), we obtain

$$(L_{\min})_x = \pi(R/V)\sigma_v \bar{G}_i(\theta) \tag{22}$$

where $\bar{G}_i(\theta) = [\cos^2\theta + 0.5\sin^2\theta]^{1/2}$, which is based on intermediate scale waves with an isotropic directional distribution (see equation (14)). Equation (22) is assumed independent of the S/C ratio. The S/C ratios for the C band SAR typically varied from 10 to 20 dB on March 11.

Equation (22) can be compared with other aircraft SAR measurements, which is useful in validating the model. Indeed, two-dimensional buoy and SAR spectra were available on March 11 [*Olsen and Barstow*, 1988], when the aircraft flew multidirectional flight paths at two altitudes over buoy 1. We select a range of R/V ratios from the March 11 data, R/V = 28, 50, 65, and 110, using two different ranges for each of the two altitudes (see passes 1 and 5 in Figure 12). The SAR spectra are given in the left and right plots, while the center plot gives the directional wave buoy spectra rotated into the radar coordinates as shown in Figures 12*a* and 12*b*. The darker the grey levels, the greater the spectral density. The two lowest R/V ratios (pass 5) are given in Figure 12*a*, and the two higher ones (pass 1) are given in Figure 12*b*. The lowest R/V (= 28) shows negligible smearing, whereas the highest R/V (= 110) shows significant smearing (azimuth low-pass filtering) as indicated by the lack of grey levels at wavelengths shorter than about 200 m along the horizontal (azimuth) wave number axis. The remaining two intermediate R/V show smearing values between those of the aforementioned cases. The significant wave height was about 4 m and the wind speed was about 8 m/s at a height of 4.2 m as measured at buoy 1. The wave systems observed during the aircraft flights were complex, with three major systems indicated by A, B, and C in both the SAR and buoy spectra. The relative change in spectral density (grey levels) between the buoy and SAR spectra is discussed by *Rufenach et al.* [this issue].

The minimum azimuth wavelength was scaled from Figure 12 for the three largest R/V ratios as given in Table 4. These $(L_{\min})_x$ values are in agreement with model values (within scaling accuracy) calculated from (22) using σ_v = 0.7 m/s [*Johnsen et al.*, this issue]. Therefore the model given by (21), after further validation, could possibly be used to estimate σ_v from two-dimensional imagery.

The minimum detectable azimuth-traveling wave is given as a function of R/V ratio in Figure 13*a* based on equation (21) for $\theta = 23°$. The minimum wavelength is displayed on the vertical axis and R/V is displayed on the horizontal axis. The curves represent different values for the velocity smearing σ_v, varying from 0.4 to 0.7 m/s, whereas the relevant R/V for ERS 1 is about 110. Therefore the range of $(L_{\min})_x$ is about 130 m for σ_v = 0.4 m/s to 260 m for σ_v = 0.7 m/s. However, directions other than azimuth are of interest. Therefore based on R/V = 110 the minimum wavelength $L_{\min}$ as a function of direction is given in Figure 13*b*. This figure is similar to Figure 13*a* except it is parameterized in ϕ_0 rather than σ_v. Figure 13*b* is based on the relationship $L_{\min} = (L_{\min})_x/\cos(\phi_0)$. For example, the minimum wavelength is 90 m to 180 m for waves traveling $\phi_0 = 45°$ to the azimuth direction. This model is a first approximation; hence as additional data and other models become available it can be updated.

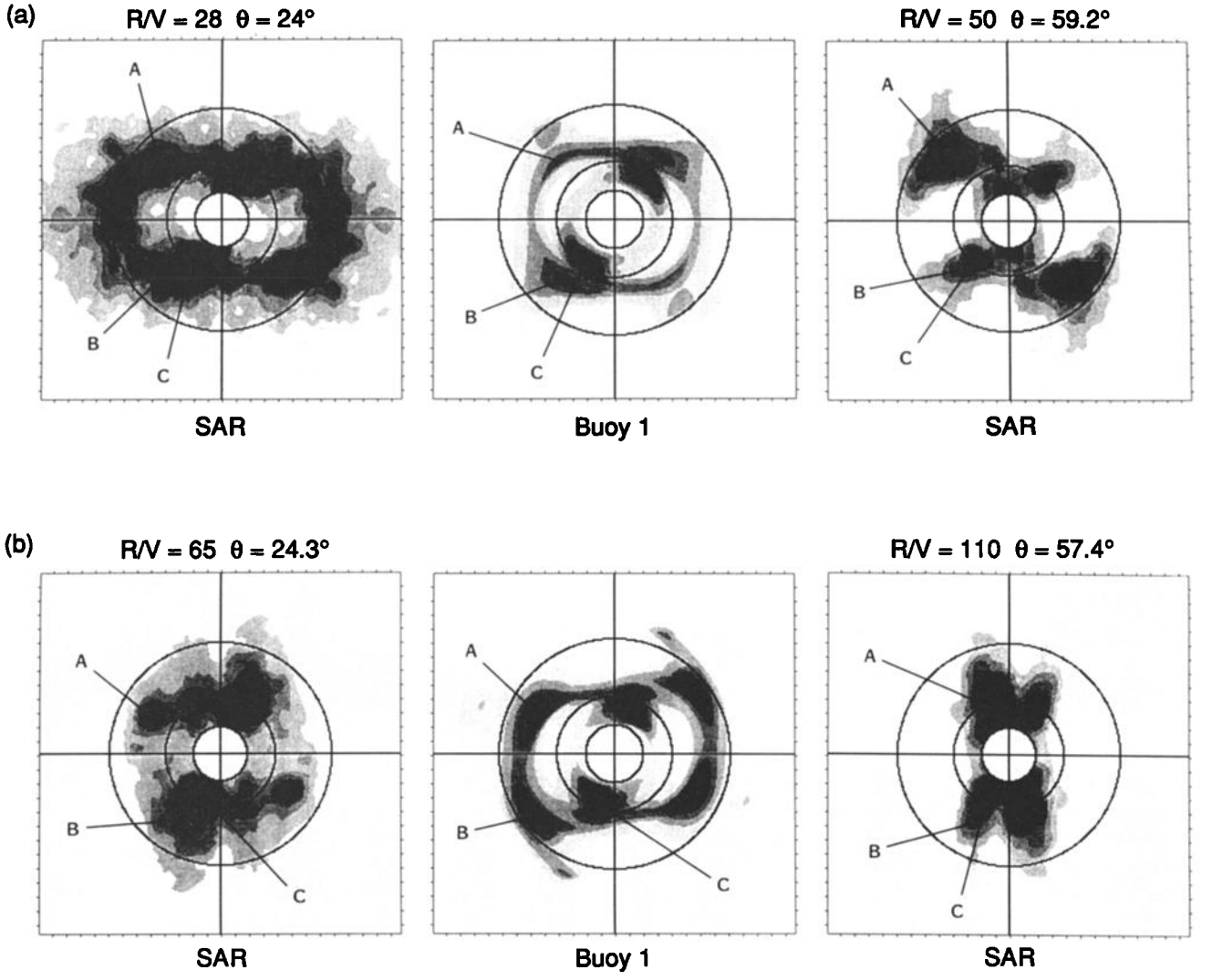

Fig. 12. SAR and buoy spectra obtained (*a*) on March 11, pass 5, at an altitude of 3650 m and (*b*) on March 11, pass 1, at 6100 m during the NORCSEX '88 experiment. The buoy spectra were rotated into the radar coordinate system. The circles indicate wavelengths of 100, 200, and 400 m, while A, B, and C indicate the locations of three wave systems. The SAR spectrum on the left side of plot is the low incidence angle, and the spectrum on the right is the high incidence angle. The center plot is the buoy spectrum. The aircraft flight direction k_x is the horizontal axis.

We assume that σ_v is dependent on wind speed with $U \approx$ 2–6 m/s corresponding to the lower values of $\sigma_v \approx 0.4$ m/s and $(L_{\min})_x \leq 150$ m. Therefore we hypothesize that ocean wave swell with peak wavelength greater than about 250 m under light winds will be imaged. This first approximation neglects velocity bunching. Higher wind speeds cause additional smearing until at sufficiently high speeds the swell waves will be completely smeared out of the image provided the swell is traveling near the spacecraft ground track.

8. Discussion

One of the objectives of the C band SAR measurements and analysis was to extract quantitative estimates of velocity smearing σ_v during NORCSEX '88 off the Norwegian coast. An attempt could then be made to apply these results to the detectability of ocean waves by the C band SAR scheduled for launch on the ERS-1 spacecraft in 1991. We obtained these estimates by processing images of ocean gravity waves into one-dimensional azimuth spectra. The width of these spectra (azimuth cutoff) were calculated using a least squares fit to a Gaussian spectral shape. Three days were selected for analysis for a range of wave heights (2 m to 5 m) and wind speeds (2 m/s to 18 m/s). The extracted σ_v values, which are independent of R/V and incidence angle, varied from 0.4 m/s to 0.7 m/s on the basis of an imaging model and

TABLE 4. March 11 Minimum Detectable Azimuth Wavelength $(L_{\min})_x$

R/V	θ, deg	$(L_{\min})_x$,* m	$\bar{G}_i(\theta)$†	$(L_{\min})_x$,‡ m
50	59.2	100	0.79	87
65	24.3	130	0.96	137
110	57.4	200	0.80	194

*Estimate scaled from two-dimensional image spectra.
†$\bar{G}_i^2(\theta) = \cos^2\theta + 0.5 \sin^2\theta$.
‡Estimate based on model given by equation (22) with $\sigma_v = 0.7$ m/s.

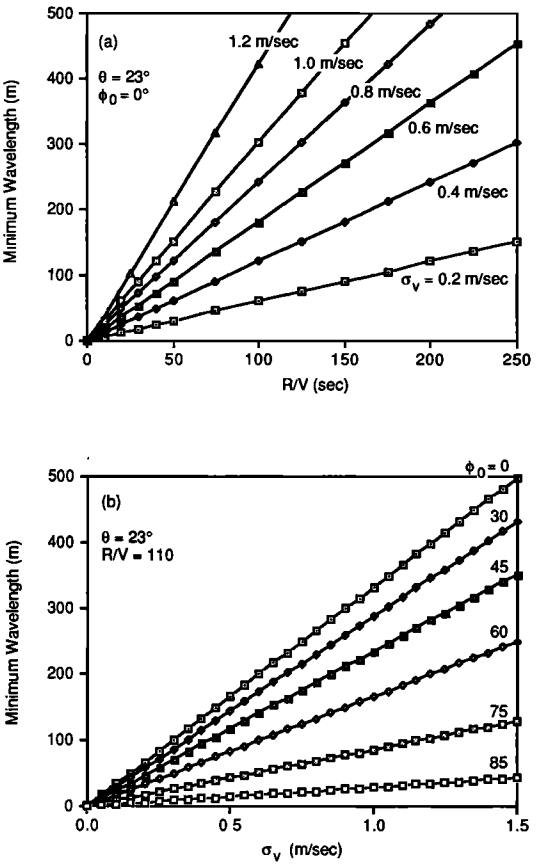

Fig. 13. Minimum detectable azimuth wavelength for the ERS 1 SAR (*a*) as a function of R/V ratio and velocity smearing σ_v based on $\theta = 23°$ and $\phi_0 = 0$, and (*b*) as a function of velocity smearing σ_v and peak wave direction ϕ_0 based on $\theta = 23°$ and $R/V = 110$.

measured azimuth cutoffs for these 3 days. This smearing model, equation (6), is fundamentally limited by the assumed form for the one-dimensional wave height spectrum in the azimuth k_x direction. The results in the present work assume a dependence k_x^{-3}, which is considered a first approximation. Future work could include the investigation of other wave height spectral forms.

The equations developed here are not based on a standard SAR two-scale model where the intermediate wavelengths are contained within a standard radar resolution cell as proposed by others [e.g., *Tucker*, 1985; *Alpers and Brüning*, 1986]. Instead, it is based on intermediate wavelengths within a degraded radar resolution cell (see equation (11)). The proposed dependence implies that increasing velocity smearing and/or nonlinear velocity bunching increases the degraded resolution, causing velocity smearing larger than the smearing within a standard (nondegraded) resolution cell.

Quantitative estimates of velocity smearing are an important input to models describing the distortion in wave imagery. Additional SAR measurements and the extracted smearing estimates are needed to better define the velocity smearing range and its dependence on environmental parameters including wind speed and significant wave height.

We investigated the dependence of velocity smearing σ_v on surface wind speed. *Tucker* [1985] and *Alpers and Brüning* [1986] gave smearing dependences on both wind speed and wave height. Their results and equation (16) in the present work are consistent with an increase in σ_v with increasing surface wind speed. The σ_v estimates extracted from the C band imagery do not show a clear dependence on wind speed from the limited measurements analyzed. The significant wave height was nearly constant, $H_{1/3} \approx 4$ m, whereas the surface wind speed U varied from ≈6 to 18 m/s on March 20 when spacecraft altimeter measurements were coaligned with the aircraft SAR measurements. This condition provided an opportunity to investigate the σ_v changes with wind speed. However, the extracted σ_v estimates and inferred wind speeds did not show a clear wind speed dependence.

The smearing within ±8 km of the boundary show significant scatter from the expected estimates. Therefore the inverse relation to wind speed at the boundary is ignored. We suggest that changes in the intermediate and/or short Bragg waves cause this observed variation.

The variation of σ_v away from the boundary shows a more systematic variation (less scatter), which implies less likelihood of a turbulence wind contribution compared to the σ_v values near the boundary. However, σ_v does not appear directly related to the surface wind speed away from the boundary unless one hypothesizes a wind saturation near, say, $U \approx 10$ m/s. Then increasing σ_v tends to be consistent with increasing U (see section 5). This proposed dependence is primarily based on the results of equation (16) and/or *Alpers and Brüning* [1986] and is physically reasonable on the basis of equation (16) provided that the low wind speeds, about 2–4 m/s, correspond to the equilibrium spectrum and wind speeds near 10 m/s correspond to a fully developed sea. That is, the smearing saturates (constant for further increase in wind speed) for a fully developed sea; i.e., $\sigma_v \approx 0.112(\rho_a')^{1/2}$ when $U \gtrsim 10$ m/s.

We use the SAR smearing increase inferred above with wind speed to propose a first-order model for the velocity smearing (azimuth cutoff) in SAR imagery. This model is valid only for the case of ocean wave swell with peak wavelength greater than about 250 m, which we assume corresponds to negligible nonlinear velocity bunching. Indeed, velocity bunching decreases with increasing peak wavelength as $\lambda_p^{-3/2}$ based on linear bunching [e.g., *Alpers*, 1983].

We use this smearing model and the C band radar-extracted σ_v values to estimate the detectability of ocean wave swell from the C band SAR scheduled for launch on the ERS 1 spacecraft in 1991. The model and the results from section 7 suggest the ocean wave swell with a peak wavelength longer than about 250 m should be imaged for light winds of about 2–4 m/s. Higher wind speeds cause additional smearing until at sufficiently high winds the swell may be completely smeared out of the image provided that it is traveling near the spacecraft ground track direction. This proposed variation could be verified using ERS 1 SAR measurements.

Acknowledgments. We thank Harald Johnsen of the Foundation of Applied Research at University of Tromso (FORUT) and David Lyzenga of Environmental Research Institute of Michigan (ERIM) for helpful discussions. This work was supported by the Norwegian Space Center, Office of Oceanographer of the Navy, SPAWAR, and the Office of Naval Research contract #N00014-81-C-0692.

REFERENCES

Alpers, W. R., Monte Carlo simulations for studying the relationship between ocean wave and synthetic aperture radar image spectra, *J. Geophys. Res.*, *88*(C3), 1745–1759, 1983.

Alpers, W. R., and C. Brüning, On the relative importance of motion-related contributions to the SAR imaging mechanism of ocean surface waves, *IEEE Trans. Geosci. Remote Sens.*, *GE-24*(6), 873–885, 1986.

Alpers, W. R., and C. L. Rufenach, The effects of orbital motion on synthetic aperture radar imagery of ocean waves, *IEEE Trans. Antennas Propag.*, *AP-27*, 685–690, 1979.

Alpers, W. R., D. B. Ross, and C. L. Rufenach, On the detectability of ocean surface waves by real and synthetic aperture radar, *J. Geophys. Res.*, *86*(C7), 6481–6498, 1981.

Banner, M. L., Equilibrium spectra of wind waves, *J. Phys. Oceanogr.*, *20*, 966–984, 1990.

Beal, R. C., D. G. Tilley, and F. M. Monaldo, Large- and small-scale spatial evolution of digitally processed ocean wave spectra from Seasat synthetic aperture radar, *J. Geophys. Res.*, *88*(C3), 1761–1777, 1983.

Brown, G. S., Estimation of surface wind speeds using satellite-borne radar measurements at normal incidence, *J. Geophys. Res.*, *84*(B8), 3974–3978, 1979.

Brüning, C., W. R. Alpers, L. F. Zambresky, and D. G. Tilley, Validation of the synthetic aperture radar ocean wave imaging theory by the shuttle imaging radar-B experiment over the North Sea, *J. Geophys. Res.*, *93*(C12), 15,403–15,425, 1988.

Donelan, M. A., J. Hamilton, and W. H. Hui, Directional spectra of wind generated waves, *Philos. Trans. R. Soc. London, Ser. A*, *315*, 509–562, 1985.

Feindt, F., V. Wismann, W. Alpers, and W. C. Keller, Airborne measurements of ocean radar cross section at 5.3 GHz as a function of wind speed, *Radio Sci.*, *21*(5), 845–856, 1986.

Hasselmann, K., R. K. Raney, W. J. Plant, W. Alpers, R. A. Shuchman, D. R. Lyzenga, C. L. Rufenach, and M. J. Tucker, Theory of synthetic aperture radar ocean imaging: A MARSEN view, *J. Geophys. Res.*, *90*(C3), 4659–4686, 1985.

Johnsen, H., K. A. Høgda, T. Guneriussen, and J. P. Pedersen, Azimuth smearing in synthetic aperture radar ocean image spectra from the Norwegian Continental Shelf Experiment of 1988, *J. Geophys. Res.*, this issue.

Keller, W. C., V. Wismann, and W. Alpers, Tower-based measurements of the ocean C band radar backscattering cross section, *J. Geophys. Res.*, *94*(C1), 924-930, 1989.

Livingstone, C. E., A. L. Gray, and R. K. Hawkins, CCRS C-band airborne radar–System description and test results, *Proc. Can. Symp. Remote Sens.*, *11th*, 503–518, June 22–25, 1987.

Lyzenga, D. R., Numerical simulation of synthetic aperture radar image spectrum for ocean waves, *IEEE Trans. Geosci. Remote Sens.*, *GE-24*(6), 863-871, 1986.

Lyzenga, D. R., An analytic representation of the synthetic aperture radar image spectrum for ocean waves, *J. Geophys. Res.*, *93*(C11), 13,859–13,865, 1988.

Lyzenga, D. R., R. A. Shuchman, J. D. Lyden, and C. L. Rufenach, SAR imaging of waves in water and ice: Evidence for velocity bunching, *J. Geophys. Res.*, *90*(C1), 1031–1036, 1985.

Olsen, R. B., and S. F. Barstow, Wave measurements on Haltenbanken during NORCSEX '88: An intercomparison of buoy, synthetic aperture radar and altimeter data, *OCEANOR Rep. OCN 88081*, pp. 1–134, Oceanogr. Co. of Norway, Trondheim, Dec. 21, 1988.

Phillips, O. M., *The Dynamics of the Upper Ocean*, p. 161, Cambridge University Press, New York, 1977.

Pierson, W. J., and L. Moskowitz, A proposed spectral form for fully developed wind seas based in the similarity theory of S. A. Kitaigorodskii, *J. Geophys. Res.*, *69*(24), 5181–5190, 1964.

Rufenach, C. L., and W. R. Alpers, Imaging ocean waves by synthetic aperture radars with long integration times, *IEEE Trans. Antennas Propag.*, AP-29, 422–428, 1981.

Rufenach, C. L., R. B. Olsen, R. A. Shuchman, and C. A. Russel, Comparison of aircraft synthetic aperture radar and buoy spectra during the Norwegian Continental Shelf Experiment of 1988, *J. Geophys. Res.*, this issue.

Schule, J. J., L. S. Simpson, and P. S. DeLeonibus, A study of fetch-limited wave spectra with an airborne laser," *J. Geophys. Res.*,*76*, 4160–4171, 1971.

Tucker, M. J., The imaging of waves by satelliteborne synthetic aperture radar: The effects of sea-surface motion, *Int. J. Remote Sens.*, *6*(7), 1059–1074, 1985.

Vesecky, J. F., and R. H. Stewart, The observation of ocean surface phenomena using imagery from the Seasat synthetic aperture radar, *J. Geophys. Res.*, 87, 3397–3430, 1982.

J. A. Johannessen, Nansen Remote Sensing Center, Edvard Griegsvei 3a, N-5037 Solheimsvik/Bergen, Norway.

N. P. Malinas, C. L. Rufenach, and R. A. Shuchman, Environmental Research Institute of Michigan, P.O. Box 8618, Ann Arbor, MI 48107.

Received November 19, 1990
revised January 30, 1991;
accepted January 23, 1991.)